NANO · MICRO
small

Supporting Information

for *Small*, DOI 10.1002/smll.202304585

Charge Storage Mechanism in Electrospun Spinel-Structured High-Entropy $(Mn_{0.2}Fe_{0.2}Co_{0.2}Ni_{0.2}Zn_{0.2})_3O_4$ Oxide Nanofibers as Anode Material for Li-Ion Batteries

Claudia Triolo, Mariam Maisuradze, Min Li, Yanchen Liu, Alessandro Ponti, Gioele Pagot, Vito Di Noto, Giuliana Aquilanti, Nicola Pinna, Marco Giorgetti* and Saveria Santangelo**

Supporting Information

Charge storage mechanism in electrospun spinel-structured high-entropy $(Mn_{0.2}Fe_{0.2}Co_{0.2}Ni_{0.2}Zn_{0.2})_3O_4$ oxide nanofibers as anode material for Li-ion batteries

Claudia Triolo, Mariam Maisuradze, Min Li, Yanchen Liu, Alessandro Ponti, Gioele Pagot, Vito Di Noto, Giuliana Aquilanti, Nicola Pinna, Marco Giorgetti*, Saveria Santangelo**

Morphology, texture, microstructure, crystalline phase and surface composition of the NFs

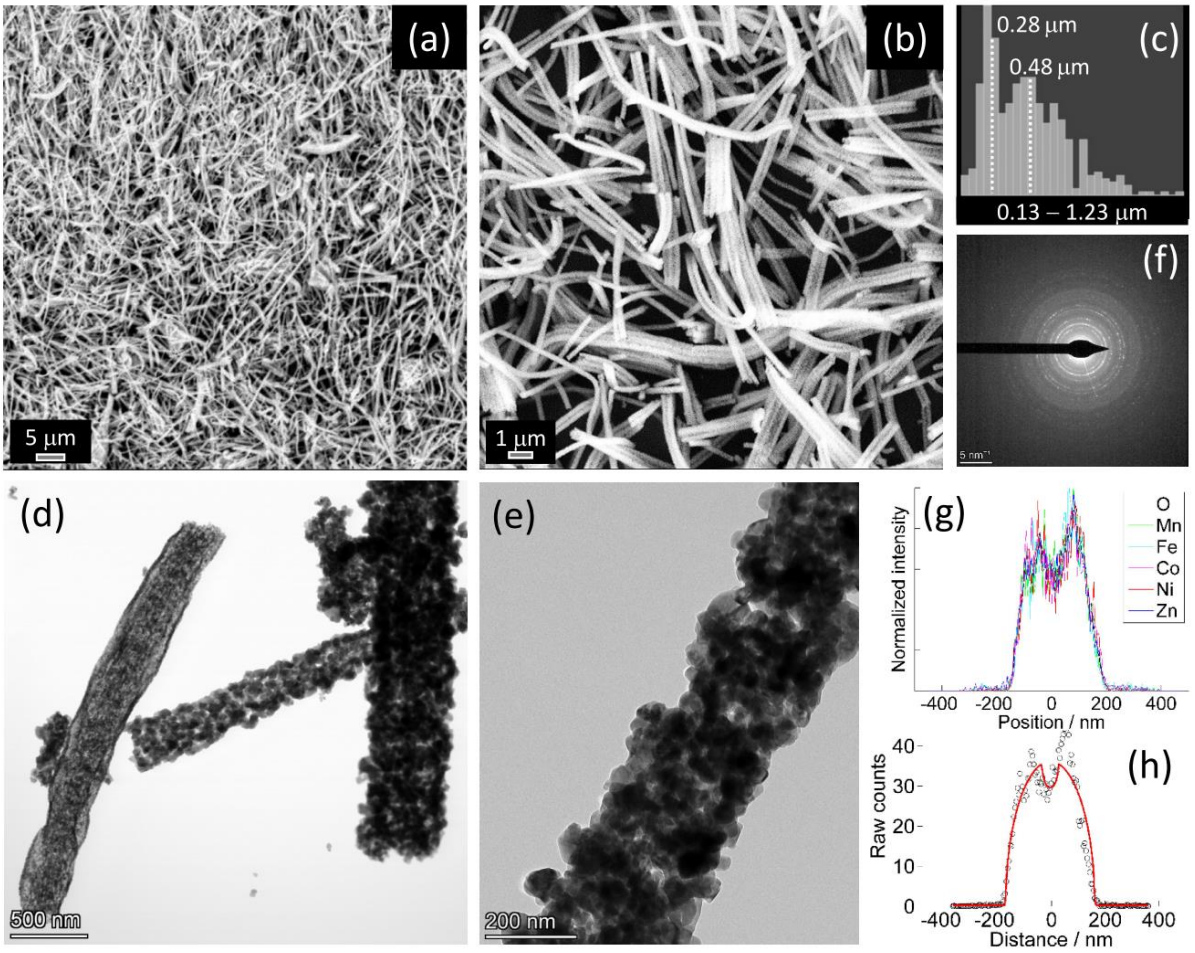

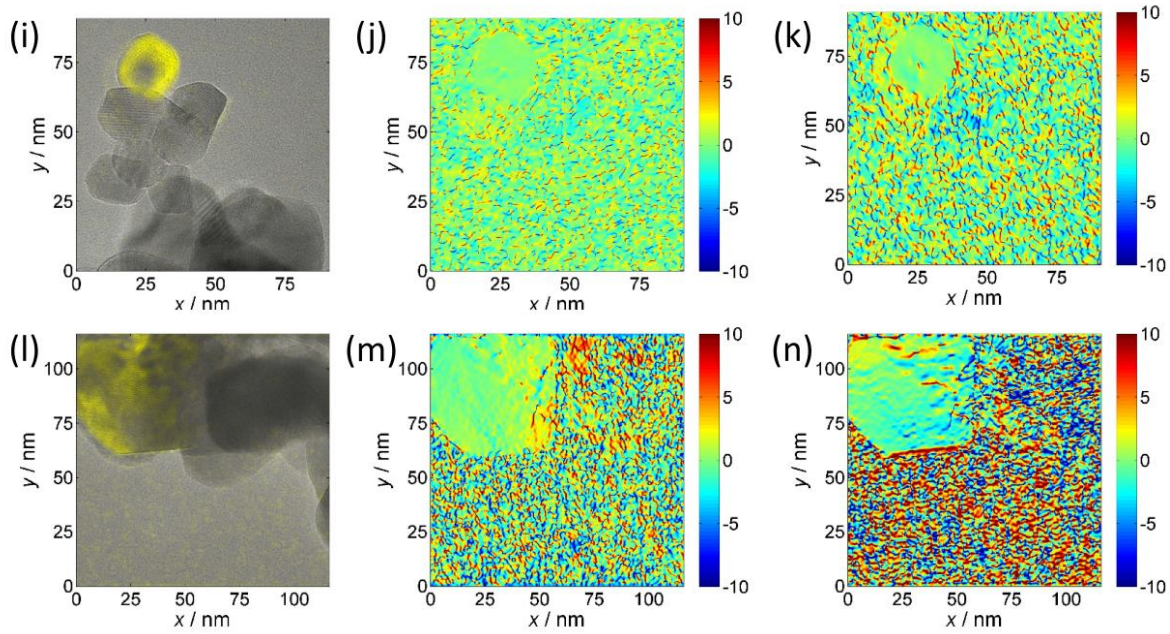

Figure S1. Results of the (a–c) SEM, (d–f) TEM and (i–n) GPA analyses. (a,b) SEM micrographs, (c) bimodal NF diameter distribution, as obtained by Fibermetric software from the SEM images, (d,e) TEM images, (f) SAED pattern for an isolated NF, (g) projection analysis of the EDX elemental maps and (h) fitting of an oxygen projected profile revealing a quasi-solid NF. (i,l) Intensity-colorized maps, (j,m) lattice rotation maps (°), and (k,n) lattice strain maps (% of cell size).

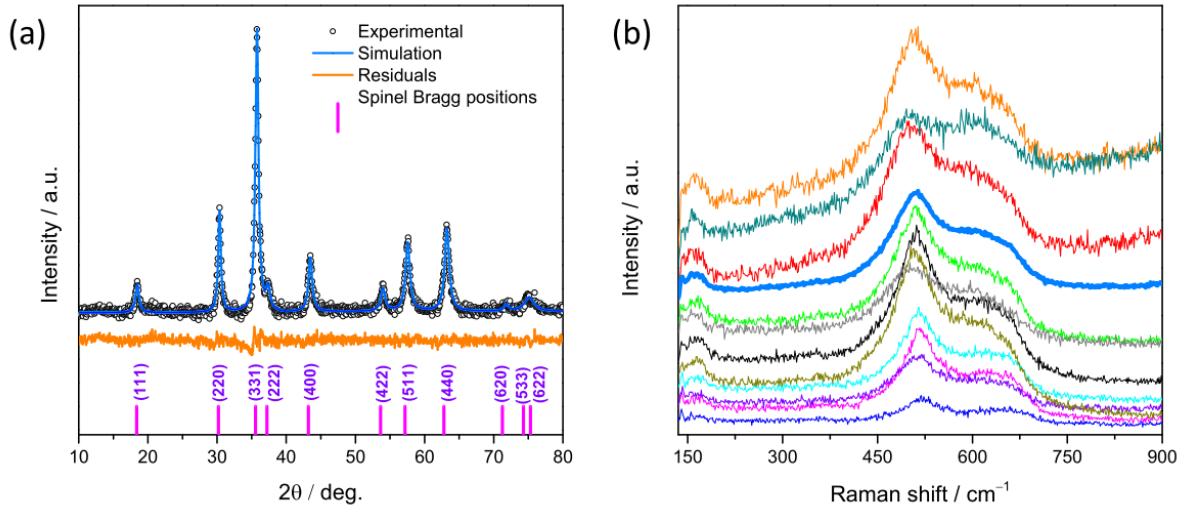

Figure S2. (a) Rietveld refinements and (b) micro-Raman spectra, as measured at different random locations, within the specimen and averaged spectrum.

Table S1. Surface elemental composition of the HEO NFs.

Mn / at.%	Fe / at.%	Co / at.%	Ni / at.%	Zn / at.%	O / at.%
5.58	1.63	6.77	4.91	6.34	74.77

Table S2. Oxygen relative composition in the HEO NFs.

O_L / at.%	O_V / at.%	ads. O / at.%
26.74	40.55	32.71

Electrochemical performance

Table S3. Results of long-term cycling stability tests on anodes based on high entropy TM oxides. The results relative to commercial graphite powders are also reported, for comparison purposes, even if operating in a different potential window. All test were carried out in CR2032-type coin-cells, at a rate of 0.5 A g^{-1}.

Active material	C additive	Binder	Electrolyte	Capacity	Cycle No.	Ref.
Spinel (Mn,Fe,Co,Ni,Zn)-HEO NFs, 70 wt%	Super P, 20 wt%	PVDF, 10 wt%	1 M $LiPF_6$ + EC + DEC, 1:1:1 v/v	155 mAh g^{-1}	550	Present work
Spinel (Cr,Mn,Fe,Co,Zn)-HEO NPs, 70 wt%	Super P, 20 wt%	PVDF, 10 wt%	1 M $LiPF_6$ + EC + DEC, 1:1:1 v/v	150 mAh g^{-1}	300	[S1]
Spinel (Cr,Mn,Fe,Co,Zn)-HEO NFs, 70 wt%	Super P, 20 wt%	PVDF, 10 wt%	1 M $LiPF_6$ + EC + DEC, 1:1:1 v/v	265 mAh g^{-1}	400	[S1]
Rock-salt (Mg,Co,Ni,Cu,Zn)-HEO NPs, 70 wt%	Super P, 20 wt%	PVDF, 10 wt%	1 M $LiPF_6$ + EC + DEC, 1:1:1 v/v	240 mAh g^{-1}	300	[S2]
Rock-salt (Mg,Co,Ni,Cu,Zn)-HEO NFs, 70 wt%	Super P, 20 wt%	PVDF, 10 wt%	1 M $LiPF_6$ + EC + DEC, 1:1:1 v/v	390 mAh g^{-1}	300	[S2]
Spinel (Mn,Fe,Co,Ni,Zn)-HEO NFs, 70 wt%	C black, 20 wt%	PVDF, 10 wt%	1 M $LiPF_6$ + EC + DEC, EC:DEC 1:1	760 mAh g^{-1}	200	[S3]
Graphite powders (Sigma-Aldrich), 80 wt%	Super P, 10 wt%	PVDF, 10 wt%	1 M $LiPF_6$ + EC + DEC, EC:DEC 1:1	125 mAh g^{-1}	300	[S4]

Ex-situ XAS analysis on the HEO-based electrode material

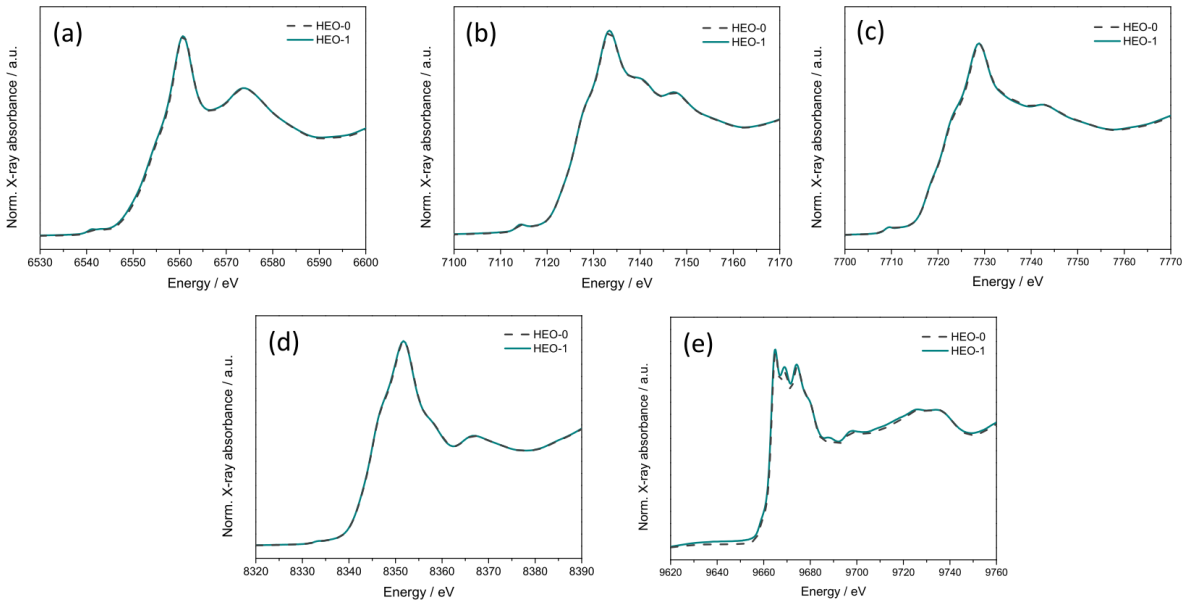

Figure S3. XANES spectra recorded at (a) Mn, (b) Fe, (c) Co, (d) Ni and (e) Zn K-edges in the fresh electrode (HEO-0) and in electrode HEO-1 (SOC: OCP).

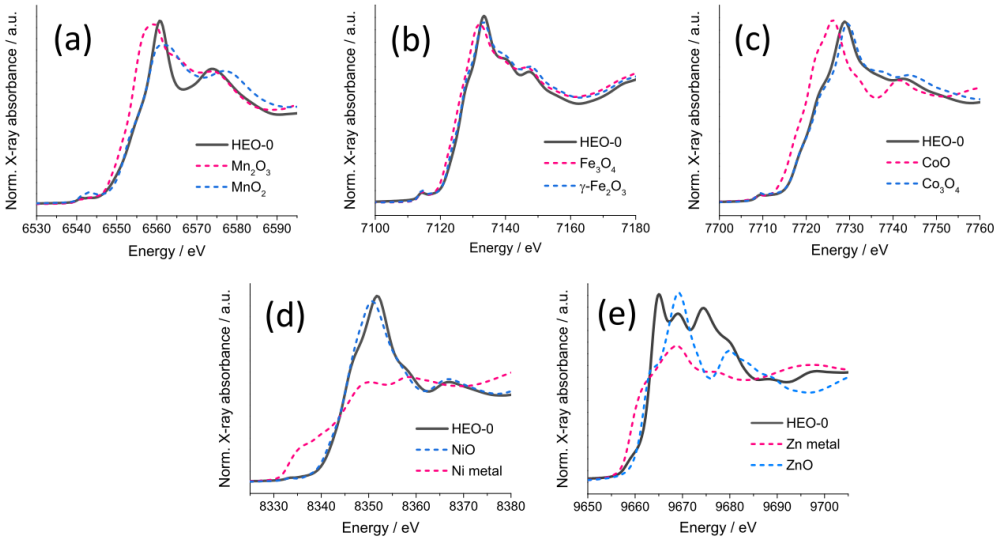

Figure S4. XANES spectra of the fresh electrode compared with metal foil and/or oxide standards for (a) Mn, (b) Fe, (c) Co, (d) Ni and (e) Zn K-edges.

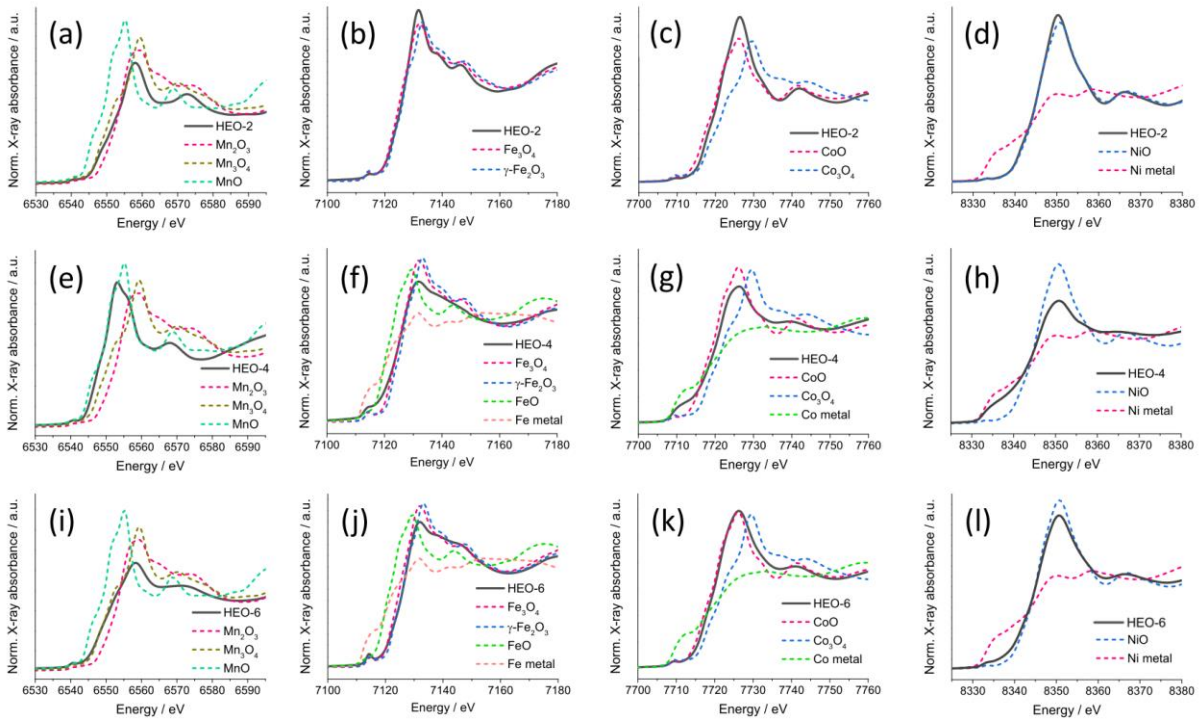

Figure S5. XANES spectra of electrodes (a–d) HEO-2, (e–h) HEO-4 and (i–l) HEO-6 compared with metal foil and/or oxide standards for (a,e,i) Mn, (b,f,j) Fe, (c,g,k) Co and (d,h,l) Ni K-edges.

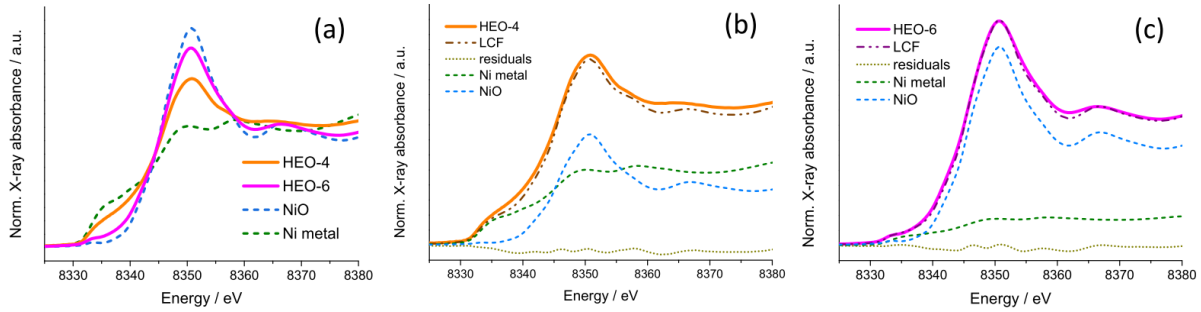

Figure S6. (a) Ni K-edge XANES spectra of electrodes HEO-4 and HEO-6 compared with metal and oxide standards; (b,c) results of LCF Ni K-edge spectra of electrodes (b) HEO-4 and (c) HEO-6.

Table S4. Outcomes of LCF for Fe, Co and Ni K-edge spectra.

Electrode	SOC	Fe				Co			Ni	
		Fe	FeO	Fe_3O_4	Fe_2O_3	Co	CoO	Co_3O_4	Ni	NiO
HEO-1	OCP	-	-	-	1	-	0.136	0.864	0.019	0.981
HEO-2	Discharge to 0.9 V	-	-	0.877	0.123	-	0.952	0.048	-	1
HEO-3	Discharge to 0.7 V	0.137	-	0.488	0.375	-	0.909	0.091	0.269	0.731
HEO-4	Discharge to 0.01 V	0.229	0.119	0.260	0.392	0.258	0.629	0.114	0.552	0.448
HEO-5	Charge to 1.4 V	0.137	-	0.488	0.375	0.159	0.694	0.147	0.484	0.516
HEO-6	Charge to 3 V	0.127	-	0.093	0.780	-	0.803	0.197	0.196	0.804
HEO-7	2^{nd} discharge to 0.01 V	0.318	0.153	0.128	0.401	0.436	0.474	0.090	0.710	0.290

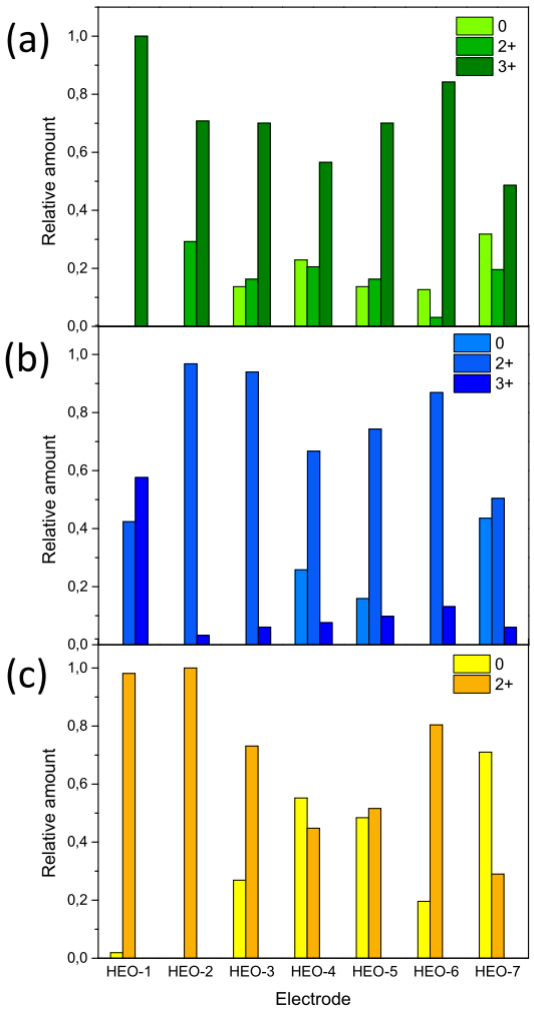

Figure S7. Relative amounts of the oxidation states of (a) Fe, (b) Co, and (c) Ni, as inferred from linear combination fitting of the corresponding K-edge spectra.

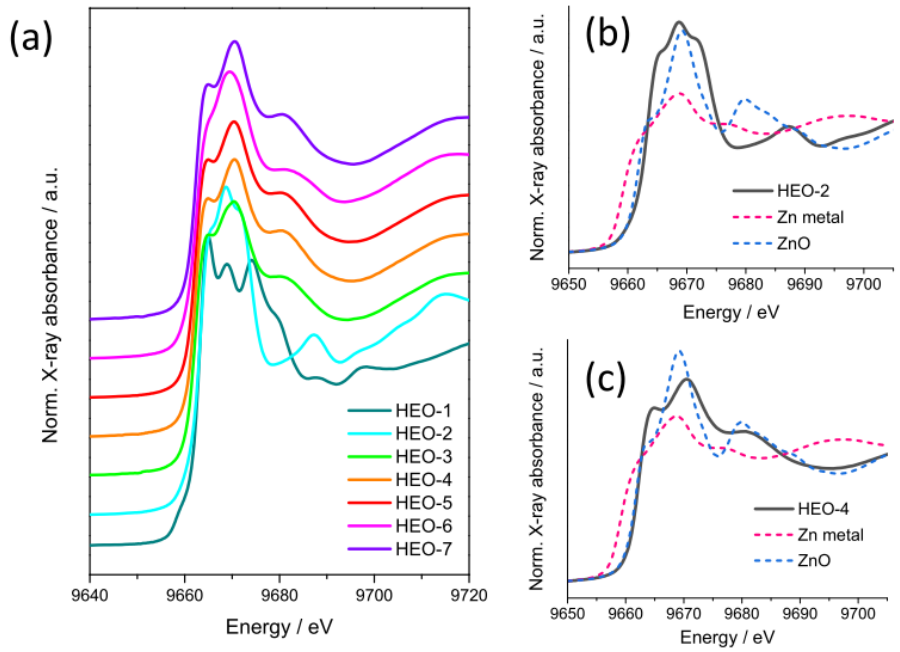

Figure S8. (a) Normalized XANES spectra recorded at Zn K-edges in electrodes with different SOC. Spectra are translated vertically for easier comparison. Comparison with Zn K-edge of metal foil and/or oxide standard for electrodes (b) HEO-2 and (c) HEO-4.

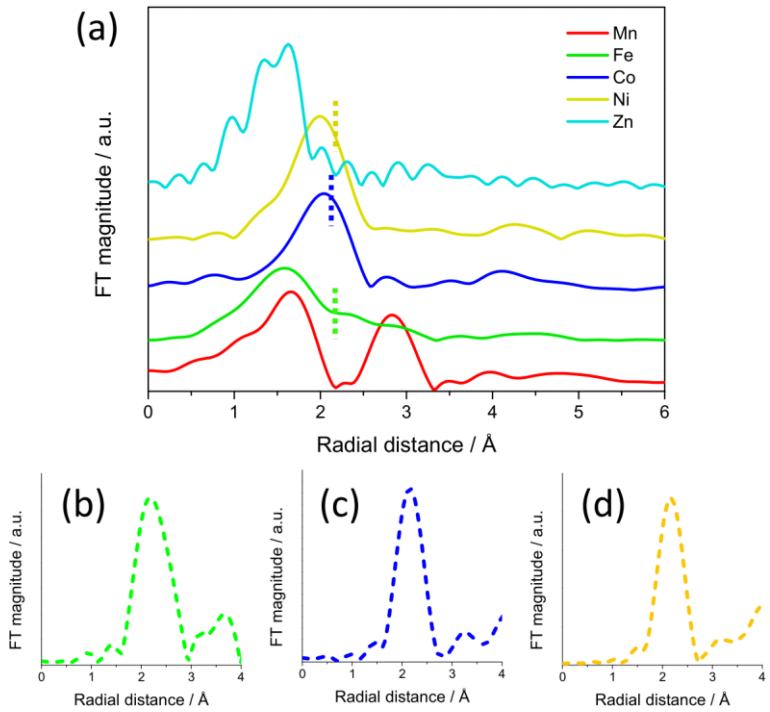

Figure S9. (a) FTs of the EXAFS for all metal K-edge in electrode HEO-7 and for K-edges of (b) Fe, (c) Co and (d) Ni metals. In panel (a), the dotted lines indicate the position of the peaks associated to the first shell in the corresponding metals.

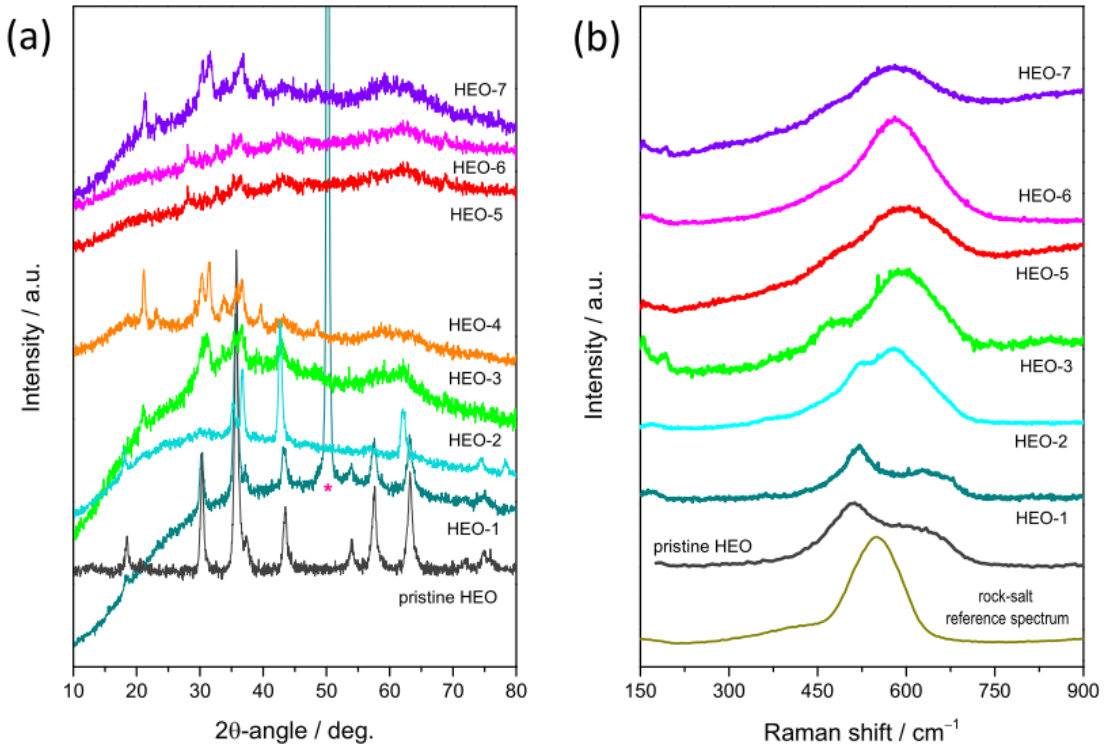

Figure 10. (a) XRD patterns and (b) averaged micro-Raman spectra of electrodes at different SOC, compared to those of pristine HEO. A star marks the XRD peak originating from the copper collector. The Raman spectra of rock-salt structured HEO is reported for comparison.

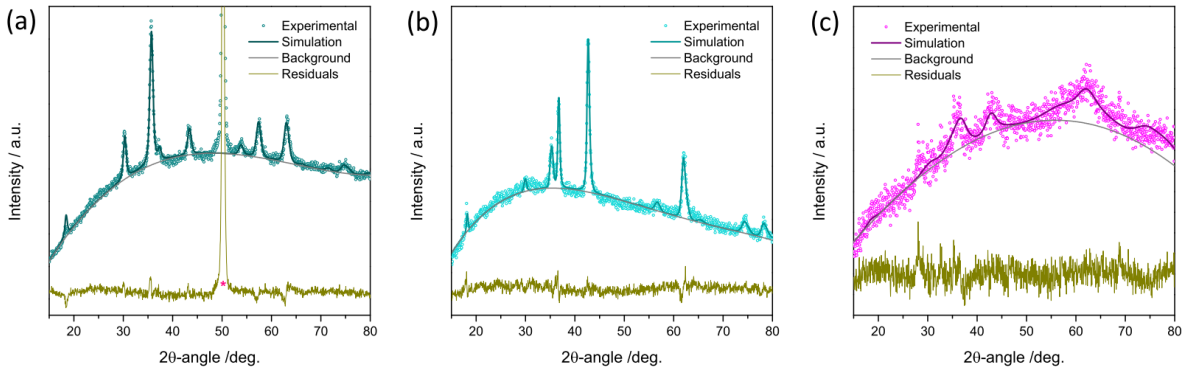

Figure 11. Rietveld refinements for electrodes (a) HEO-1, (b) HEO-2 and (c) HEO-6. A star marks the XRD peak originating from the copper collector.

Table S5. Results of Rietveld refinements Results of Rietveld refinements for electrodes HEO-1, -2, and -6.

Electrode	Phase	Cell side *a* / Å	RMS microstrain	Weight %
HEO-1	Spinel	8.302 ± 0.003	0.0092 ± 0.0004	
HEO-2	Spinel	8.435 ± 0.003	0.0078 ± 0.0007	33 ± 5
	Rock-salt	4.2365 ± 0.0004	0.0031 ± 0.0003	67 ± 5
HEO-6	Spinel	8.30 ± 0.03	0.05 ± 0.01	25 ± 25
	Rock-salt	4.22 ± 0.01	0.021 ± 0.007	72 ± 25

[a)] Crystallite size = 20 ± 2 nm. The crystallite size for HEO-2 and -6 electrodes has high statistical uncertainty and is therefore not reported.

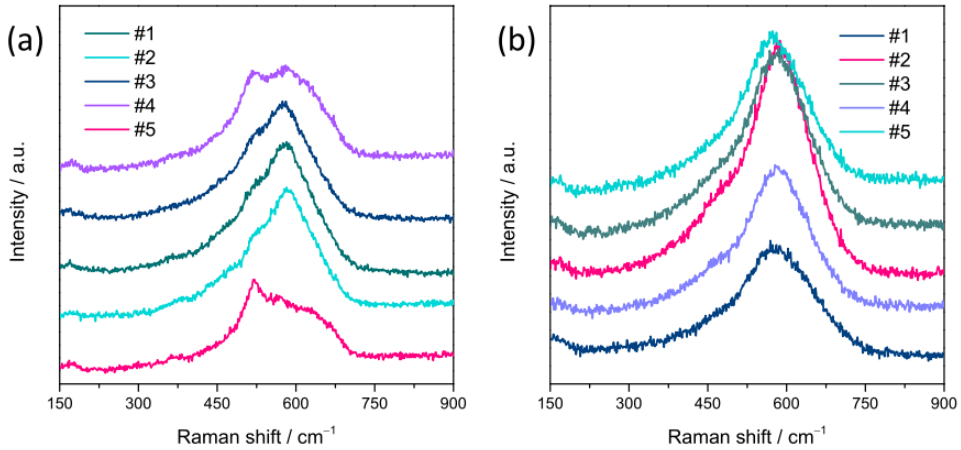

Figure S12. Micro-Raman spectra, as measured at different random locations, within electrodes (a) HEO-2 and (b) HEO-6.

Distribution of cations in the pristine NFs

Table S6. Cation site occupancy in the pristine NFs at thermal equilibrium.

Cation	8*a*		16*d*		
	2+	3+	2+	3+	4+
Mn					0.75
Fe		0.24		0.06	
Co			0.45	0.15	
Ni			0.60		
Zn	0.75				

Table S7. Cation site occupancy in the pristine NFs for the completely random case.

Cation	8a			16d		
	2+	3+	4+	2+	3+	4+
Mn			0.25			0.50
Fe		0.10			0.20	
Co	0.15	0.05		0.30	0.10	
Ni	0.20			0.40		
Zn	0.25			0.50		

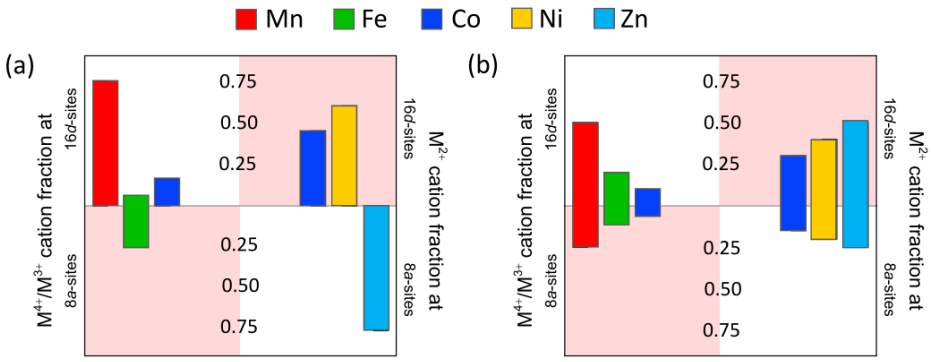

Figure S13. (a) Equilibrium distribution of cations and (b) completely random distribution of cations. The cation distribution in the present NFs is expected to be between these two distributions.

Synthesis of the (Mn,Fe,Co,Ni,Zn)-HEO NFs

The (Mn,Fe,Co,Ni,Zn)-HEO NFs were synthesized by electrospinning (ES) followed by calcination in air. A 7.14 % by weight polyacrylonitrile (PAN, CAS No. 25014-41-9, Sigma Aldrich) in 9.1 g *N*,*N*-dimethylformamide (DMF, CAS No. 68-12-2, Sigma Aldrich) solution was first prepared. After stirring the solution at 350 rpm for 1 h at room temperature (RT), stoichiometric amounts of the acetates (Table S7) were added, one at a time, under continuous stirring to obtain a homogeneous solution containing an equimolar combination of Mn, Fe, Co, Ni and Zn with 38.46 wt% (relative to PAN) total amount of metals. After slow mixing overnight at RT, the solution was loaded into a 20 mL syringe equipped with a 40 mm long, 0.8 mm gauge stainless steel needle. ES was operated via a CH-01 Electro-spinner 2.0 (Linari Engineering s.r.l.) at 25 ± 1 °C and 40–45% relative air humidity, under a DC voltage of 15–16 kV, applied over a distance of 15 cm between the tip of the needle and the grounded collector. The solution was fed at a rate of 18.8 μL min^{-1}.

Most of DMF very rapidly evaporated during the ES. The PAN/(Mn,Fe,Co,Ni,Zn)-acetates NFs, collected in the form of a non-woven membrane over an aluminum foil, were allowed to dry at RT overnight. Then, peeling from the collector, they were calcined in static air. During this process, the organic components of the as-spun precursor NFs were completely removed and HEO-NFs were generated through the combustion reaction $3\,Mn(CH_3COO)_2 + 3\,Fe(CH_3COO)_2 + 3\,Co(CH_3COO)_2 + 3\,Ni(CH_3COO)_2 + 3\,Zn(CH_3COO)_2 + 62.5\,O_2 \rightarrow 5\,(Mn_{0.2}Fe_{0.2}Co_{0.2}Ni_{0.2}Zn_{0.2})_3O_4 + 45\,H_2O + 60\,CO_2$.

Table S8. CAS numbers, suppliers and stoichiometric amounts of the metal salts dissolved in the polyacrylonitrile /*N*,*N*-dimethylformamide spinnable solution.

Metal source	CAS No.	Supplier	Amount / g
$Mn(CH_3COO)_2{\cdot}4H_2O$	6156-78-1	Sigma Aldrich	0.1078
$Fe(CH_3COO)_2$	3094-87-9	Sigma Aldrich	0.0765
$Co(CH_3COO)_2{\cdot}4H_2O$	6147-53-1	Sigma Aldrich	0.1096
$Ni(CH_3COO)_2{\cdot}4H_2O$	6018-89-9	Sigma Aldrich	0.1095
$Zn(CH_3COO)_2{\cdot}2H_2O$	5970-45-6	Fischer Scientific	0.0966

Projection analysis of the EDX elemental maps and GPA

Detailed information on the NF inner morphology is obtained via projection analysis of STEM-EDX maps. A straight, constant-diameter NF (or region of a NF) is selected, and the oxygen map intensity is integrated (projected) along the NF axis. NF segments of length 420 to 770 nm are integrated. Then, the resulting transverse projection is fitted to

$$I_{hollow} = I_{background} + I_0 \left(\sqrt{1-(r/R_{out})^2} - \sqrt{1-(r/R_{in})^2}\right)$$

where $I_{\text{background}}$ and I_0 denote the projected background intensity and a constant depending on the NF size and composition, respectively, r is the distance from the NF axis, and R_{out} and R_{in} indicate the outer and inner diameter of a hollow NF, respectively.

Structural information about the primary particles is inferred by the geometrical phase analysis (GPA) of lattice fringes proposed by Hÿtch [S5]. The HRTEM images are Fourier transformed (FT), and the peaks were assigned to the reciprocal vectors $\mathbf{g}_{hkl}$ of the spinel lattice. For each peak, the 2D FT image is filtered by an isotropic Gaussian filter and inverse FT-ed to real space as a complex image. The intensity ($Re^2 + Im^2$) image highlights the regions of the HRTEM image where the $\mathbf{g}_{hkl}$ fringes are present. The phase of the complex image is further processed following ref. [S6] to produce the lattice rotation and Lagrange strain maps, corresponding to $\mathbf{g}_{hkl}$. As a result, three separate images are obtained: (i) the original black-and-white HRTEM image colorized with yellow hue proportional to the lattice fringe amplitude; (ii) the rotation map, expressed as rotation in degree from $\mathbf{g}_{hkl}$; (iii) the Lagrange strain map, expressed as percentage deviation of the imaged interplanar distance from $1/|\mathbf{g}_{hkl}|$.

References

[S1] B. Petrovičovà, W. Xu, M. G. Musolino, F. Pantò, S. Patanè, N. Pinna, S. Santangelo, C. Triolo, *Appl. Sci.* **2022**, *12*, 5965.

[S2] C. Triolo, W. Xu, B. Petrovičovà, N. Pinna, S. Santangelo, *Adv. Funct. Mater.* **2022**, 32, 2202892.

[S3] C. Y. Huang, C. W. Huang, M. C. Wu, J. Patra, T. X. Nguyen, M. T. Chang, O. Clemens, J. M. Ting, J. Li, J. K. Chang, W. W. Wu, *Chem. Eng. J.* **2021**, *420*, 129838.

[S4] J. Kim, S. M. N. Jeghan, G. Lee, *Microporous Mesoporous Mater.* **2020**, *305*, 110325.

[S5] M. J. Hÿtch, *Microsc. Microanal. Microst.* **1997**, 8, 41.

[S6] J. L. Rouvière, E. Sarigiannidou, *Ultramicroscopy* **2005**, 106, 1.